RSC Advances

PAPER

View Article Online
View Journal | View Issue

Cite this: *RSC Adv.*, 2025, **15**, 38346

Simultaneous strength and ductility improvement of As-cast HfMoTaTiZrCr$_x$ refractory high entropy alloys *via* Cr addition

Man Xu,[a] Lei Bai,[a] Xiang Guo,[b] Huihui Wang,[a] Kyungjun Lee,[c] Zijian Geng[bd] and Junjun Wang *[a]

Received 16th July 2025
Accepted 19th September 2025

DOI: 10.1039/d5ra05085e

rsc.li/rsc-advances

Overcoming the strength-ductility trade-off in refractory-based high-entropy alloys (RHEAs) is challenging. In this work, simultaneous strength-ductility enhancement of as-cast HfMoTaTiZrCr$_x$ refractory high-entropy alloys (RHEAs) was attained through Cr addition. Experimental results reveal that Cr addition induces a unique triphasic microstructure, comprising a Hf/Ti/Zr-enriched BCC1 phase, a Mo/Ta-dominated BCC2 phase, and a Cr/Mo/Ta-dominated C15-type Laves phase. The optimized HfMoTaTiZrCr$_{0.75}$ alloy achieves $\sigma_{0.2}$ of 1982.7 MPa (28% higher than Cr-free HfMoTaTiZr RHEAs) and ε_f of 12.4% (65% enhancement), representing an outstanding strength among reported as-cast RHEAs with comparable ductility. Microstructural analysis suggests that the uniformly distributed BCC phase redistributes compressive stress and suppresses crack propagation, while the Laves phase enhances strength through Laves phase-induced dislocation obstruction.

1. Introduction

Traditional alloys, primarily composed of a single base element with minor alloying additions, face inherent limitations in achieving multifunctional performance for extreme engineering applications,[1–3] such as aerospace components, military armour systems, and propulsion units. The emergence of high-entropy alloys (HEAs) revolutionized metallurgical paradigms,[4,5] introducing an innovative design framework that unlocks unprecedented compositional flexibility and multi-property optimization through multi-principal element interactions, enabling outstanding mechanical robustness and resistance to harsh operational conditions.[1,3,6] In contrast to conventional alloys, HEAs demonstrate superior mechanical performance, including synergistic enhancements in strength and fracture resistance.[7–10]

Refractory high-entropy alloys (RHEAs), leveraging multi-principal element interactions, have emerged as transformative candidates for use in extreme conditions due to their high melting points and outstanding mechanical properties.[11] The WNbMoTa RHEA reported by Senkov *et al.*[12] exhibits a disordered BCC_A2 structure with a yield strength of 1058 MPa but has a limited room temperature (RT) fracture strain of 2.1%. To overcome the brittleness of MoNbTaVW RHEA, Senkov *et al.*[13] developed the HfNbTaTiZr RHEA by substituting W/Mo/V with Hf//Ti/Zr, which exhibits a compressive yield strength of 929 MPa along with an impressive ductility exceeding 50% at RT. Subsequent work by Juan *et al.*[14] extended this approach to design HfMoTaTiZr RHEA, maintaining single-phase BCC structures with RT yield strength reaching 1600 MPa and fracture strains of 4%. Such trade-offs between strength and ductility limit their application in extreme environments, where catastrophic failure under loading must be avoided. Recent advances in phase engineering strategies—particularly the introduction of Laves phases *via* chromium (Cr) alloying—offer a pathway to resolve this dilemma. Guo *et al.*[15] and Geng *et al.*[16] achieved concurrent strength-ductility enhancement in as-cast AlCrMoNbTi and Al$_{0.5}$Mo$_{0.5}$NbTa$_{0.5}$TiZr RHEA *via* Cr addition, respectively. Last year, Bai *et al.*[17] demonstrated that incorporating Cr into the HfMoTaTiZr significantly enhances its mechanical properties. Specifically, the HfMoTaTiZrCr$_{0.5}$ RHEA showed a remarkable increase of 207.5 MPa in compressive yield strength and a 20.6% improvement in fracture deformation rate compared to its parent HfMoTaTiZr RHEA reported by Juan *et al.*[14] This observation was also corroborated by Wang *et al.*[18] However, while the addition of Cr has been shown to improve the mechanical properties of HfMoTaTiZr alloys, there is a lack of in-depth studies on the relationship between Cr content, the phase, and structural evolution of HfMoTaTiZrCr$_x$

[a]*Hubei Key Laboratory of Plasma Chemistry and Advanced Materials, School of Materials Science and Engineering, Engineering Research Center of Environmental Materials and Membrane Technology of Hubei Province, Wuhan Institute of Technology, Wuhan 430074, P.R. China. E-mail: junjunwang@wit.edu.cn*

[b]*State Key Laboratory of Advanced Technology for Materials Synthesis and Processing, Wuhan University of Technology, Wuhan 430070, P.R. China*

[c]*Department of Mechanical Engineering, Gachon University, Gyeonggi Seongnam Seongnam, Gyeonggi & Incheon, South Korea*

[d]*Department of Mechanical and Energy Engineering, Southern University of Science and Technology, Shenzhen 518055, P.R. China*

RHEAs. Further research is necessary to understand these aspects and achieve enhanced performance.

In this work, we systematically investigate the role of Cr addition in as-cast $HfMoTaTiZrCr_x$ ($x = 0$, 0.5, 0.75, 1, 1.25, and 1.5) RHEAs, focusing on phase engineering strategies to balance strength and ductility. The HfMoTaTiZr and $HfMoTaTiZrCr_{0.5}$ alloys have been investigated in our previous study.[17] Selected data, such as their microstructure and mechanical properties, from this prior work are intentionally reused in this work to establish baseline comparability with the newly developed Cr-alloyed systems ($HfMoTaTiZrCr_x$, x = 0.75, 1, 1.25, and 1.5) under identical processing conditions. This controlled data recurrence enables precise evaluation of the interaction between the secondary BCC phase and intermetallic Laves phase and their influence on mechanical properties. The underlying mechanism is also discussed to explain the simultaneous improvement of strength and ductility.

2. Experimental

Atomic radius and melting point of elements Hf, Mo, Ta, Ti, Zr and Cr are summarized in Table 1. The $HfMoTaTiZrCr_x$ (x = 0∼1.5) alloys were synthesized *via* vacuum arc-melting using high-purity raw metals (>99.95 wt%) under Ar atmosphere. To achieve compositional homogeneity, each ingot underwent five remelting cycles, and the nominal compositions and compositions measured by inductively coupled plasma optical emission spectroscopy (ICP-OES, PerkinElmer 8300) are listed in Table 2, indicating the design and measured compositions are in good agreement.

Phase identification of as-cast $HfMoTaTiZrCr_x$ was performed *via* X-ray diffraction (XRD, Empyrean, Malvern Panalytical) using Cu Kα radiation with a step size of 0.02° over a 2θ range of 20–90°. Thin foils with electron transparency for TEM observation were prepared by focused ion beam (FIB). The foil samples were then examined using a transmission electron microscope (TEM) (Thermo Scientific FEI Talos F200X, USA). Microstructural characterization was conducted with a field-emission scanning electron microscope (FEI Quanta 250) coupled with energy-dispersive X-ray spectroscopy (Oxford X-Act EDS) to analyze phase morphology and elemental distribution. Vickers microhardness testing (Innovatest Falcon 401AM) was performed at room temperature under a 0.3 kgf load with a 15-second indentation, with five replicate tests per specimen. For compressive property assessment, cylindrical specimens (Ø3 × 6 mm) were tested at room temperature using an Instron 5967 servo-hydraulic system with a crosshead displacement rate of 0.008 mm s^{-1} (initial strain rate $\varepsilon = 0.001\ s^{-1}$).

Table 1 Atomic radius and melting point of primary elements in $HfMoTaTiZrCr_x$

	Hf	Mo	Ta	Ti	Zr	Cr
Melting point (°C)	2227	2622	3007	1670	1854	1907
Atomic radius (Å)	1.59	1.39	1.46	1.47	1.60	1.28

3. Results and discussion

3.1. Microstructure

XRD patterns of as-cast $HfMoTaTiZrCr_x$ (x = 0∼1.5) RHEAs are shown in Fig. 1. The diffraction peaks of Cr-free RHEA ($x = 0$, HfMoTaTiZr) are indexed to be a single-phase BCC structure, aligning with the observation in literature.[14] Upon the addition of 9.1 at% Cr (Cr0.5), additional diffraction peaks emerged, which correspond to two BCC phases (denoted as BCC1 and BCC2) and a cubic C15 Laves phase ($MgCu_2$-type). Cross-referencing with prior reports on HfMoTaTiZr-based systems suggests it is likely to be a Cr–X (X = Ti, Zr, Hf, and Ta) Laves phase.[19–23] With increasing Cr content, the peak of the BCC1 phase gradually shifts to low two theta angles, while BCC2 showed an opposite trend, indicating that BCC1 exhibits a larger lattice parameter than BCC2. Concurrently, the Laves phase exhibited progressively enhanced diffraction intensity, accompanied by the emergence of secondary Laves phase diffraction peaks at higher Cr contents, revealing an increase in its volume fraction in as-cast $HfMoTaTiZrCr_x$.

Fig. 2 presents SEM backscatter electron (BSE) contrast images of the as-cast microstructure of $HfMoTaTiZrCr_x$ RHEAs. All alloys exhibit a typical as-cast dendritic structure characterized by pronounced microsegregation, forming two distinct

Table 2 Nominal and measured composition of as-cast $HfMoTaTiZrCr_x$ (in at%)

RHEAs/designations	Compositions	Hf	Mo	Ta	Ti	Zr	Cr
HfMoTaTiZr (Cr0)	Nominal	20.00	20.00	20.00	20.00	20.00	0.00
	Measured	19.92	20.33	20.28	19.84	19.63	0.00
$HfMoTaTiZrCr_{0.5}$ (Cr0.5)	Nominal	18.18	18.18	18.18	18.18	18.18	9.10
	Measured	17.99	18.57	18.66	17.88	17.97	8.93
$HfMoTaTiZrCr_{0.75}$ (Cr0.75)	Nominal	17.39	17.39	17.39	17.39	17.39	13.05
	Measured	17.18	17.96	18.01	17.07	16.96	12.82
$HfMoTaTiZrCr_1$ (Cr1)	Nominal	16.67	16.67	16.67	16.67	16.67	16.65
	Measured	16.48	17.27	17.19	16.41	16.38	16.27
$HfMoTaTiZrCr_{1.25}$ (Cr1.25)	Nominal	16.00	16.00	16.00	16.00	16.00	20.00
	Measured	15.98	16.63	16.52	15.55	15.72	19.60
$HfMoTaTiZrCr_{1.5}$ (Cr1.5)	Nominal	15.38	15.38	15.38	15.38	15.38	23.10
	Measured	15.16	15.88	16.03	15.17	14.93	22.83

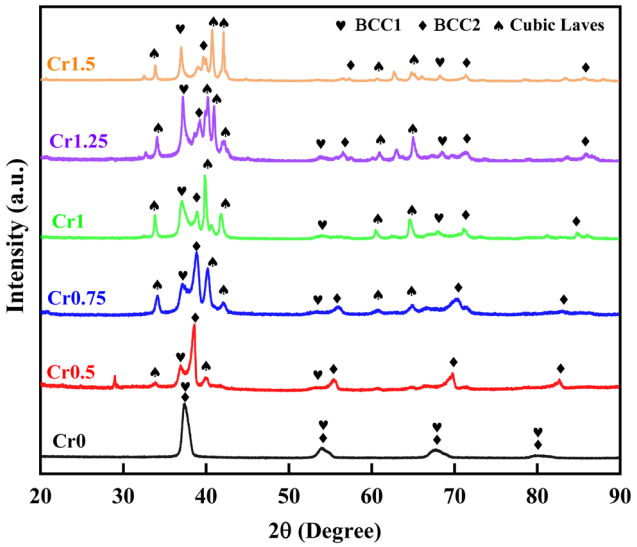

Fig. 1 XRD patterns of as-cast $HfMoTaTiZrCr_x$ RHEAs.

regions: dendritic and interdendritic. Specifically, in the Cr-free alloy (Cr0), both the bright dendritic cores (D) and gray interdendritic zones (ID) are identified as BCC-structured phases (Fig. 2). Notably, the Cr0.5 alloy reveals the nucleation of fine granular Laves phase particles (black contrast) within ID regions, accompanied by dendritic expansion relative to the Cr0 base alloy. Further Cr additions trigger a morphological evolution of Laves phases—from discrete granular precipitates in Cr0.5 to irregular flaky morphologies at higher Cr contents. Consequently, the area of the DR gradually decreases, while the ID region and the irregular flake Laves phase progressively expand. Eventually, the D region becomes surrounded by the gray ID regions, with localized nucleation of flake Laves phase precipitates at ID-region cores. This microstructural progression highlights the BCC/Laves phase spatial interplay: the BCC1 phase preferentially distributes in dendritic regions, while the Laves phase (Cr/Mo/Ta-dominated) nucleates within interdendritic zones. Their complementary spatial arrangement (Fig. 2c) establishes a load-bearing network, where the ductile BCC phase accommodates strain while the hard Laves phase resists deformation, synergistically enhancing mechanical properties.

Table 3 presents the chemical compositions of D and ID regions in as-cast $HfMoTaTiZrCr_x$ alloys, quantified *via* energy-dispersive spectroscopy (EDS). The D region of these RHEAs is enriched in high melting-point elements, specifically Mo (2622 °C) and Ta (3007 °C), while the ID is enriched with relatively low melting-point elements, namely Hf (2227 °C), Ti (1670 °C), and Zr (1854 °C). The Cr content is low in both the D and ID regions, generally below 10 at%. In contrast, Cr is highly concentrated in the Laves phase, with its content reaching approximately 28 at%. Notably, the Laves phase, predominantly located in the ID regions, exhibits high Mo and Ta concentrations, suggesting these elements serve as primary constituents. Additionally, significant Hf and Zr contents were detected in this phase. Although binary phase diagrams indicate that Mo and Cr cannot form cubic Laves phases,[24] the work by Gao *et al.*[25] demonstrates that Mo can incorporate into the Cr-based Laves structure based on two key factors: (1) the calculated Mo–Cr mixing enthalpy approaches zero based on the Miedema's semi-empirical model, and (2) atomic radius matching of Cr and Mo, leading to limited impact on lattice strain. These findings support the Mo substitution in the sublattice sites of the Laves phase for Cr atoms. Consequently, the chemical formula of the

Table 3 Chemical compositions (in at%) of D and ID regions in as-cast $HfMoTaTiZrCr_x$ alloys, quantified *via* EDS

Alloys and regions			Hf	Mo	Ta	Ti	Zr	Cr
Cr0	D	BCC	16.4	23.7	29.0	18.2	12.7	0
	ID	BCC	21.7	18.0	16.3	20.9	23.1	0
Cr0.5	D	BCC2	13.2	27.0	32.1	15.4	8.3	4.1
	ID	BCC1	22.0	11.0	8.4	22.9	31.3	4.5
		Laves	16.8	17.3	9.2	11.9	16.3	28.5
Cr0.75	D	BCC2	12.6	26.8	31.9	15.6	7.4	5.7
	ID	BCC1	21.3	13.4	9.0	24.6	25.8	5.9
		Laves	17.2	16.8	13.5	11.3	14.4	26.8
Cr1	D	BCC2	12.1	27.1	32.0	15.7	5.9	7.2
	ID	BCC1	20.3	11.7	16.2	26.5	21.0	4.4
		Laves	17.0	16.9	16.1	10.7	13.1	27.6
Cr1.25	D	BCC2	10.7	27.4	33.4	14.3	5.6	9.1
	ID	BCC1	16.9	6.6	7.4	24.1	28.3	16.7
		Laves	17.1	18.4	15.7	10.2	12.0	26.6
Cr1.5	D	BCC2	9.6	26.3	32.6	15.8	5.5	10.3
	ID	BCC1	17.5	5.8	9.3	33.5	30.0	3.9
		Laves	16.6	15.5	14.3	12.4	12.4	28.8

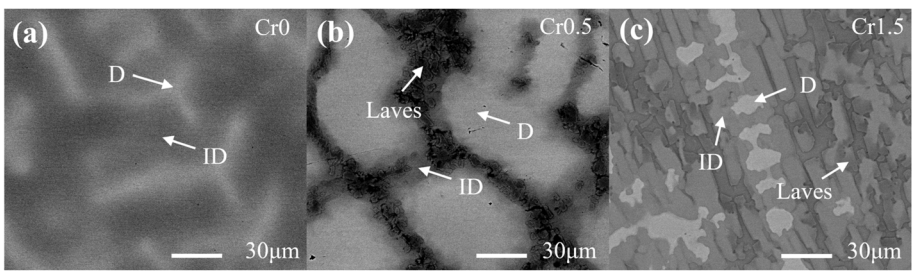

Fig. 2 Backscattered electron (BSE) micrographs illustrating the microstructural evolution of as-cast $HfMoTaTiZrCr_x$ alloys with varying Cr content: (a) Cr-free baseline ($x = 0$), (b) intermediate Cr addition ($x = 0.5$), and (c) high Cr concentration ($x = 1.5$). Note: microstructural data for HfMoTaTiZr and $HfMoTaTiZrC_{0.5}$ in panels (a and b), originally reported in our previous work,[17] are strategically reused here to enable direct quantification of chromium's compositional effects.

cubic Laves phase can be temporarily represented as (Cr, Mo)$_2$(Hf, Ta, Ti, Zr).

TEM observations further corroborate the conclusions drawn from XRD analysis. Fig. 3 presents the TEM bright-field micrographs, selected area electron diffraction (SAED) patterns of HfMoTaTiZr RHEA, and the corresponding elemental distribution map. The single-phase HfMoTaTiZr exhibits a uniform element distribution without any observable segregation. The EDS image in Fig. 4a reveals three distinct elemental distributions within the Cr0.5 and Cr1.5 alloys, *i.e.*, regions I, II, and III, with notable variations in the distribution of Mo, Ta, Ti, Zr, and Cr. The SAED patterns from regions I and II indicate that both correspond to the BCC phase, aligning with the Cr0 RHEA. However, compared to region I, region II contains lower concentrations of Ta and Mo. These observations suggest that regions I and II are BCC1 and BCC2 phases, respectively. A comparative analysis of XRD patterns and TEM micrographs shows that the incorporation of Cr causes significant lattice contraction for the BCC2 phase, which exhibits a 17.5% volume reduction at $x = 1.5$ (Table 4). The SAED pattern identified region III as the C15 type Laves phase, a low-temperature stabilized Laves phase typically observed in Cr–Hf/Ta/Ti/Zr systems compared to the C14 and C36 polymorphs. TEM-EDS analysis reveals that this Laves phase is predominantly composed of Cr, Mo, and Ta, with a certain amount of Hf, Ti, and Zr—a phenomenon that has also been observed in other studies of alloys containing Hf, Mo, Ti, and Zr.[26–28]

The observation by TEM analysis and thermodynamic rules further supports the proposed formula of the C15 Laves phase as (Cr, Mo)$_2$(Hf, Ta, Ti, Zr). First, Cr exhibits a strong thermodynamic tendency to form Laves phases with Hf, Ti, Zr, and Ta, such as Cr_2Hf, Cr_2Zr, Cr_2Ti, and Cr_2Ta,[29] while Hf, Zr, Ti, and Ta are fully miscible and do not form intermetallic compounds. Thus, it is rational that Cr mainly occupies the A site, while Hf, Zr, Ti, and Ta mainly occupy the B site in the C15 Laves phase. For Mo atoms, their smaller atomic radii compared to Hf, Zr, Ti, and Ta—similar to Cr—result in a limited impact on lattice strain. Therefore, it is reasonable that Mo also mainly enters the A sites.

The above results indicate that adding Cr in HfMoTaTiZr RHEA significantly impacts the solidification process, which modifies the solidification path and affects phase formation and the microstructure. During solidification, as the system tends to minimize its Gibbs free energy, elements with higher melting points will tend to solidify earlier and form primary phases, *i.e.*, the dendrites,[13] which is confirmed by the observation in Fig. 2 and 3 that dendrites are dominated by elements

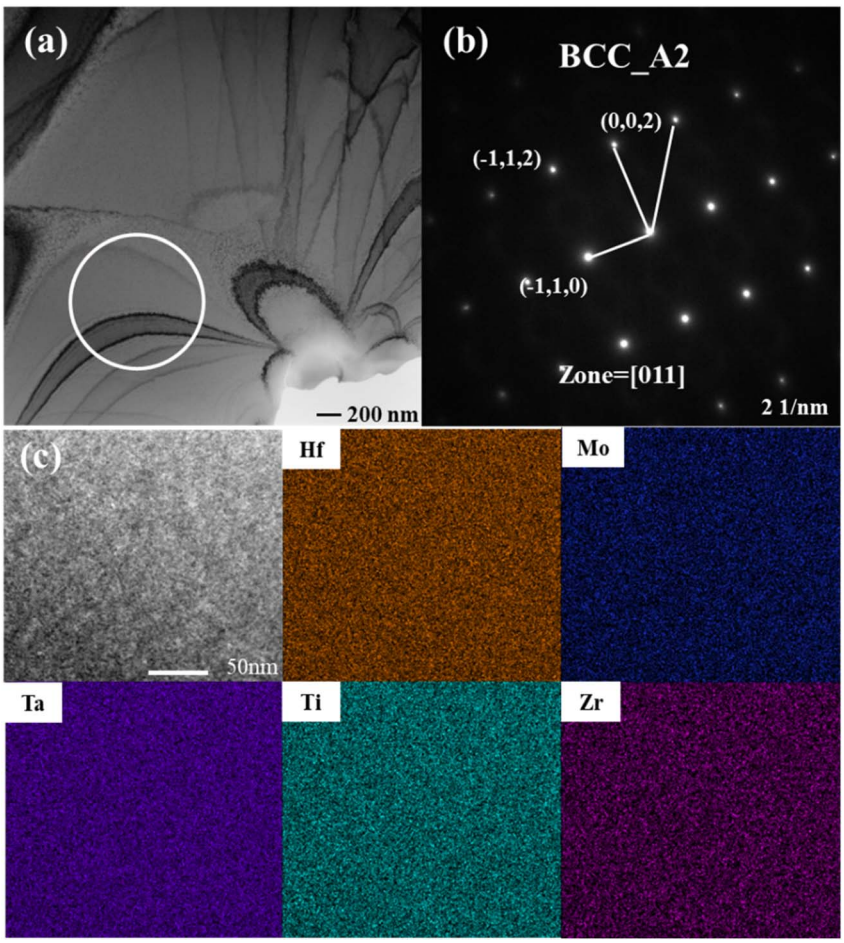

Fig. 3 (a) Bright-field TEM image (b) selective area electron diffraction pattern and (c) corresponding elemental distribution maps of HfMoTaTiZr RHEA.

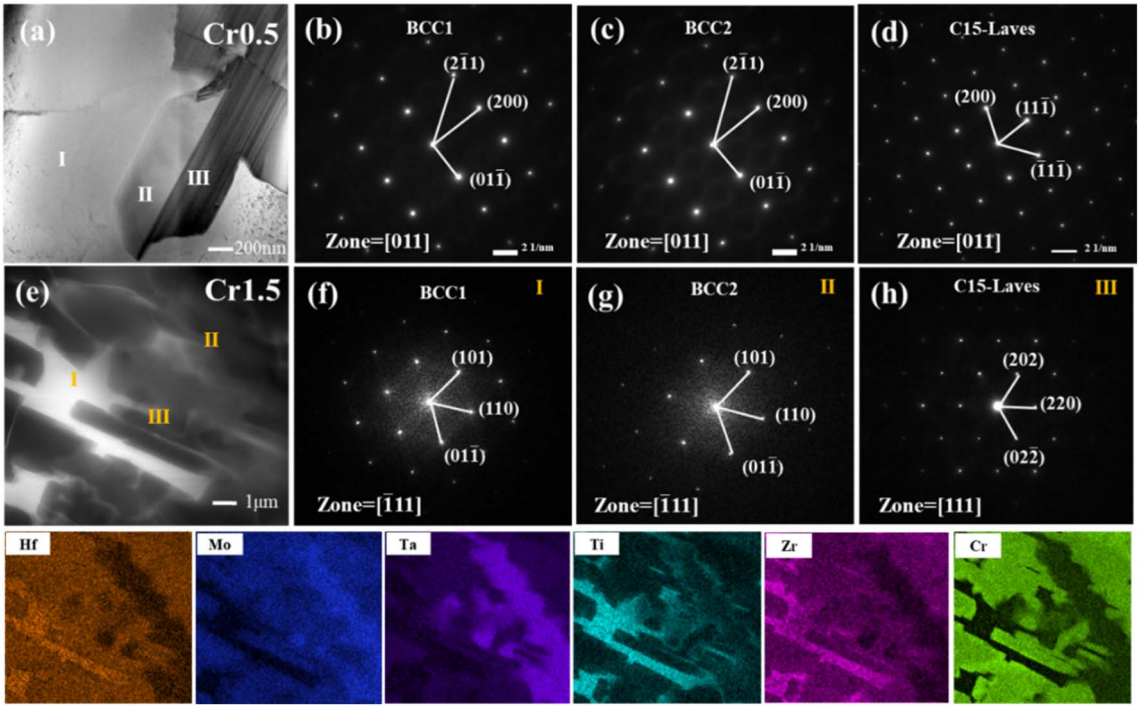

Fig. 4 Bright-field TEM image, corresponding elemental distribution maps and selective area electron diffraction patterns of areas I, II, and III of (a–d) $HfMoTaTiZrCr_{0.5}$ RHEA, (e–h) $HfMoTaTiZrCr_{1.5}$.

Table 4 Measured lattice constants and unit cell volumes of the BCC phase and the C15 type Laves phase in HfMoTaTiZr, $HfMoTaTiZrCr_{0.5}$ and $HfMoTaTiZrCr_{1.5}$ RHEAs

Alloys	Phases	Analysis methods	Lattice constants (Å)	Volume (Å^3)
Cr0	BCC	XRD	3.39	38.96
		TEM	3.43	40.35
Cr0.5	BCC1	XRD	3.44	40.71
		TEM	3.42	40.00
	BCC2	XRD	3.32	36.59
		TEM	3.29	35.61
	Laves	XRD	7.49	420.19
		TEM	7.49	420.19
Cr1.5	BCC1	XRD	3.46	41.42
		TEM	3.50	42.88
	BCC2	XRD	3.18	32.16
		TEM	3.24	34.01
	Laves	XRD	7.48	418.51
		TEM	7.29	387.42

with higher melting-points (Mo and Ta). Elements with lower melting points will remain in the liquid phase longer and become enriched in the remaining liquid. Thus, in $HfMoTaTiZrCr_x$ RHEAs, the solidification process drives elemental partitioning, concentrating lower-melting-point elements (Hf, Zr, Ti, Cr) in the residual liquid phase. This segregation behavior, coupled with Cr's strong thermodynamic tendency to form Laves phases with Hf/Ti/Zr,[19] promotes the nucleation of C15-type Laves precipitates in as-cast $HfMoTaTiZrCr_x$ RHEA. Similar behavior was also observed in $Al_{0.5}Mo_{0.5}NbTa_{0.5}TiZrCr_x$ RHEAs.[16]

3.2. Mechanical properties

Fig. 5 presents the Vickers hardness for $HfMoTaTiZrCr_x$ RHEAs. The addition of Cr significantly enhances the Vickers hardness of these RHEAs. Specifically, the hardness increases from 460 to 704 $HV_{0.3}$ as the Cr content rises, with the Cr1.5 RHEA exhibiting the highest hardness, representing a 52% improvement compared to Cr0. The observed hardness enhancement directly correlates with the elevated volume fraction of the C15-Laves phase. It is speculated that this Laves phase with large unit cells and complex atomic arrangements impedes dislocation movement through dislocation pinning more effectively than simpler BCC/FCC structures. The precipitation of Laves phase induces lattice distortions in the adjacent matrix due to atomic size mismatch, synergistically enhancing both solid-solution

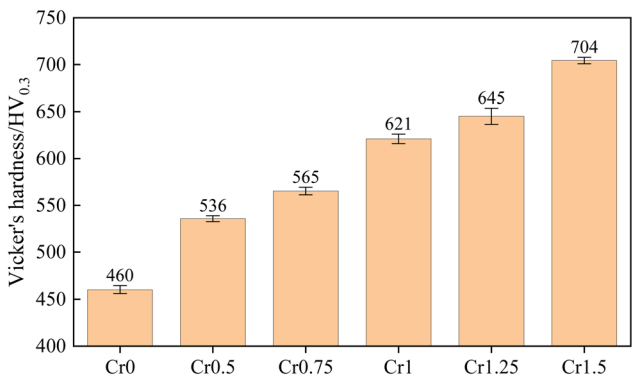

Fig. 5 Vicker's hardness of $HfMoTaTiZrCr_x$ ($x = 0\sim1.5$) RHEAs.

and precipitation strengthening effects. Furthermore, the Laves phase is adjacent to the matrix BCC phase, where phase boundaries act as obstacles to dislocation movement, requiring greater energy for dislocations to traverse. These factors collectively make the Laves phase a critical contributor to the increased hardness of $HfMoTaTiZrCr_x$ RHEAs.

Fig. 6 presents the RT compressive stress–strain curves of as-cast $HfMoTaTiZrCr_x$ RHEAs. The derived compression yield strength ($\sigma_{0.2}$) and fracture strain (ε_f) are summarized in Table 5. For Cr0 RHEA, $\sigma_{0.2}$ and ε_f are 1543.1 MPa and 7.5%, respectively, which closely align with the room temperature $\sigma_{0.2}$ of 1600 MPa reported for the same alloy in the literature. As the Cr content increases, both $\sigma_{0.2}$ and ε_f increase simultaneously, until reaching 1982.7 MPa and 12.4% at Cr0.75, which exhibits the outstanding strength among reported as-cast RHEAs with comparable ε_f (*e.g.*, 1719 MPa and 10% for MoNbHfZrTi; 1746 MPa and 11% for $Al_xHfNbTiZr$; 1677 MPa and 9% for MoNbCrVTi, 1746 MPa and 7% for $Al_{0.5}Mo_{0.5}NbTa_{0.5}TiZrCr$, 1992 MPa and 8% for $AlCr_{1.8}MoNbTi$).[15,16,30–33] Beyond this point, $\sigma_{0.2}$ continues to increase, attaining a maximum of 2003.0 MPa at Cr1, while ε_f declines with further Cr additions. As shown in Fig. 6a, $HfMoTaTiZrCr_x$ RHEAs with relatively lower Cr content, *i.e.*, Cr0, Cr0.5, and Cr0.75, exhibit plastic fracture characteristics, while Cr1, Cr1.25, and Cr1.5 show typical brittle fracture behavior. Considering the highest $\sigma_{0.2}$ and ε_f, it can be concluded that 0.75 is the optimum Cr content for $HfMoTaTiZrCr_x$ RHEAs. We speculated that the simultaneous strength-ductility improvement in the Cr0.75 alloy arises from the synergistic interplay between the BCC and Laves phases. The ductile BCC1 phase accommodates plastic deformation through dislocation glide, effectively absorbing strain energy and delaying crack initiation. Concurrently, the hard Laves phase enhances load-bearing capacity by redistributing external stresses *via* interfacial stress transfer between the BCC and Laves phases. This dual mechanism—plasticity-dominated BCC phase, load-bearing Laves phase, collectively underpins the exceptional mechanical synergy in the Cr0.75 RHEAs. However, at $x > 0.75$, the Laves phase volume fraction increases substantially, creating a continuous brittle network. This morphological shift promotes early crack initiation and propagation under strain, as the hard Laves phases no longer act as isolated strengtheners but instead as stress concentrators. This mirrors observations in AlCrMoNbTi RHEAs,[15] where exceeded Laves phases caused similar ductility drops.

Table 5 RT yield strength ($\sigma_{0.2}$) and fracture strain (ε_f) of as-cast $HfMoTaTiZrCr_x$ RHEAs

Designations	$\sigma_{0.2}$ (MPa)	ε_f (%)
Cr0	1543.1	7.5
Cr0.5	1779.6	11.1
Cr0.75	1982.7	12.4
Cr1	2003.0	8.2
Cr1.25	1964.7	7.3
Cr1.5	1662	6.1

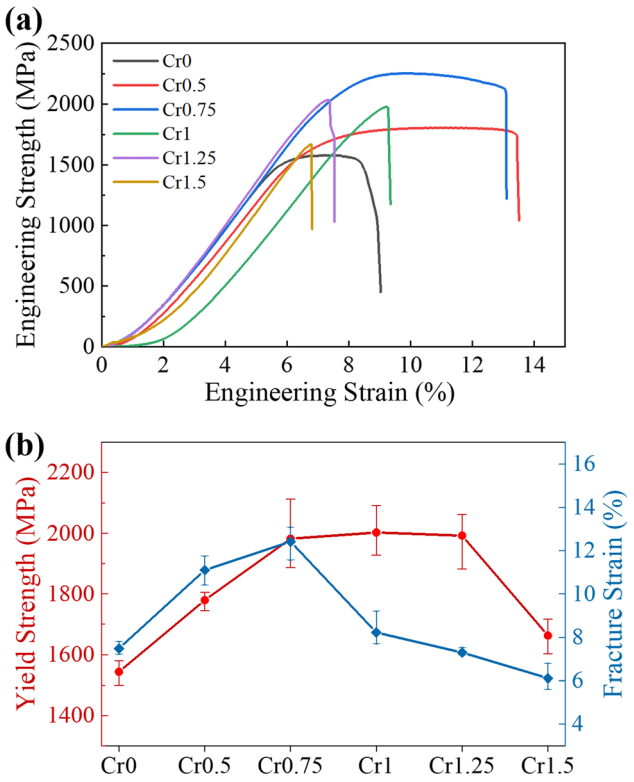

Fig. 6 (a) RT compressive stress–strain curves of as-cast $HfMoTaTiZrCr_x$ ($x = 0$, 0.5, 0.75, 1, 1.25, 1.5) RHEAs and (b) the derived $\sigma_{0.2}$ and ε_f at different Cr content. Note: data for HfMoTaTiZr and $HfMoTaTiZrC_{0.5}$, originally reported in our previous work,[17] are strategically reused here to enables direct quantification of chromium's compositional effects.

Despite the intrinsic brittleness of Laves phases, the present study indicates that their formation can contribute to an increase in the compression fracture strain of an alloy—a phenomenon also observed in a previous study.[34] Under compressive loading, materials generally exhibit higher strain tolerance than tensile loading, because compressive stress helps prevent the crack initiation and propagation, which is the dominant failure mechanism in brittle Laves phases. The formation of Laves phases thus enhances the material's ability to resist deformation under compression, allowing it to withstand higher strains before failure. Moreover, Laves phases, being hard and strong, are capable of bearing a significant portion of the load within the alloy. When these phases are well-distributed, they help to redistribute the applied compressive stress throughout the material. This redistribution reduces localized stress concentrations, enabling the alloy to deform more uniformly under compression and achieve a higher ultimate strain. Moreover, the Laves phase can act as a barrier to crack propagation; cracks that initiate within the softer matrix may be arrested or deflected by the Laves phases, preventing catastrophic failure and allowing the material to absorb more strain before fracturing.

Fracture surfaces of $HfMoTaTiZrCr_x$ RHEAs are presented in Fig. 7. While Cr0 exhibits the characteristics of intergranular fracture and cleavage fracture, the Cr0.5 alloy shows not only distinct cleavage planes but also numerous dimples. Comparative analysis between HfTaTiZr[35] and HfMoTaTiZr[36] reveals

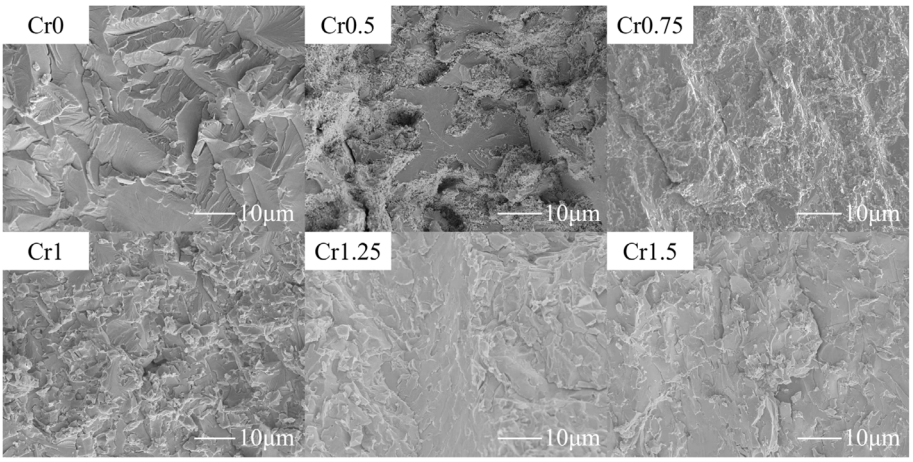

Fig. 7 Fracture surfaces of HfMoTaTiZrCr$_x$ RHEAs.

that the Mo-rich HfMoTaTiZr alloy possesses inferior ductility. Based on these observations, the fracture mechanism can be rationalized as follows: the BCC2 phase (Hf/Ti/Zr-enriched) exhibits superior plasticity compared to the Mo/Ta-dominated BCC1 phase. Cracks preferentially nucleate in the brittle BCC1 regions and then propagate through the BCC2 phase along specific crystallographic planes or slip systems, thereby retarding crack propagation. However, with increasing Cr content (Cr1, Cr1.25, and Cr1.5 alloys), the formation of abundant Laves phases leads to predominantly brittle fracture features.

4. Conclusions

Cr addition drives significant phase transformation and microstructural refinement in as-cast HfMoTaTiZrCr$_x$ RHEAs. The Cr-free HfMoTaTiZr RHEA exhibits a disordered BCC_A2 structure. In contrast, Cr incorporation induces a triphasic architecture comprising Hf/Ti/Zr-enriched BCC1, Mo/Ta-rich BCC2, and a C15-type Laves phase chemically approximated as (Cr, Mo)$_2$(Hf, Ta, Ti, Zr). Cr additions amplify the Laves phase fraction, synergistically enhancing hardness (+52%, 460 to 704 HV$_{0.3}$), yield strength ($\sigma_{0.2}$), and fracture strain (ε_f) *via* Laves phase-mediated dislocation blocking and compressive stresses redistribution by newly formed and uniformly distributed BCC1 phase. The optimized HfMoTaTiZrCr$_{0.75}$ RHEA achieves impressive compressive properties ($\sigma_{0.2}$ = 1982.7 MPa, ε_f = 12.4%) among reported as-cast RHEAs with comparable ductility. Beyond this optimal composition, $\sigma_{0.2}$ peaks at 2003.0 MPa (Cr$_1$), while ε_f declines due to excessive brittle Laves phase. Future studies will employ *in situ* mechanical testing coupled with high-resolution microscopy to directly observe crack–interface interactions, further elucidating the dynamic deformation mechanisms in these multiphase RHEAs.

Author contributions

Man Xu: supervision, writing – review and editing. Lei Bai: investigation, methodology, writing – original draft. Xiang Guo: investigation, methodology, writing – original draft. Huihui Wang: writing – review and editing, Kyungjun Lee: writing – review and editing. Zijian Geng: investigation, formal analysis, methodology. Junjun Wang: supervision, conceptualization, formal analysis, writing – review and editing.

Conflicts of interest

The authors declare that they have no known competing financial interests or personal relationships that could have appeared to influence the work reported in this paper.

Data availability

All key graphical data supporting this study are included in the main body of this article. Additional raw test data obtained during this research are available on Baidu Netdisk at **https://pan.baidu.com/s/1Eml7uam_aYa2rko9NbXUNg** with the accession number of 1234.

Acknowledgements

The authors gratefully acknowledge the financial support from the Natural Science Research Project for Young Talents of Department of Education of Hubei Province (Project Number: 20242088), the Scientific Research Foundation of Wuhan Institute of Technology (Project Number K2023081), and the Wuhan Talent Program - Outstanding Youth Project (Grant Number 20232375).

References

1 E. P. George, D. Raabe and R. O. Ritchie, *Nat. Rev. Mater.*, 2019, **4**, 515–534.
2 W. Xiong, A. X. Y. Guo, S. Zhan, C.-T. Liu and S. C. Cao, *J. Mater. Sci. Technol.*, 2023, **142**, 196–215.
3 F. D. C. Garcia Filho, R. O. Ritchie, M. A. Meyers and S. N. Monteiro, *J. Mater. Res. Technol.*, 2022, **17**, 1868–1895.

4 J. W. Yeh, S. K. Chen, S. J. Lin, J. Y. Gan, T. S. Chin, T. T. Shun, C. H. Tsau and S. Y. Chang, *Adv. Eng. Mater.*, 2004, **6**, 299–303.
5 S. Wu, Z. Li, J. He, F. Zhang, L. Wang, L. Zhang and X. Cheng, *Def. Technol.*, 2025, **50**, 236–253.
6 K. K. Alaneme, M. O. Bodunrin and S. R. Oke, *J. Mater. Res. Technol.*, 2016, **5**, 384–393.
7 C. Xu, L. Fang, G. Xu, L. Yang, Y. Ouyang and X. Tao, *J. Alloys Compd.*, 2024, **990**, 174390.
8 O. N. Senkov, G. B. Wilks, J. M. Scott and D. B. Miracle, *Intermetallics*, 2011, **19**, 698–706.
9 X. Shen, Z. Guo, F. Liu, F. Dong, Y. Zhang, C. Liu, B. Wang, L. Luo, Y. Su, J. Cheng, X. Yuan and P. K. Liaw, *J. Alloys Compd.*, 2024, **990**, 174459.
10 Y. Fu, J. Li, H. Luo, C. Du and X. Li, *J. Mater. Sci. Technol.*, 2021, **80**, 217–233.
11 O. N. Senkov, D. B. Miracle, K. J. Chaput and J.-P. Couzinie, *J. Mater. Res.*, 2018, **33**, 3092–3128.
12 O. N. Senkov, G. B. Wilks, D. B. Miracle, C. P. Chuang and P. K. Liaw, *Intermetallics*, 2010, **18**, 1758–1765.
13 O. N. Senkov, J. M. Scott, S. V. Senkova, D. B. Miracle and C. F. Woodward, *J. Alloys Compd.*, 2011, **509**, 6043–6048.
14 C.-C. Juan, M.-H. Tsai, C.-W. Tsai, C.-M. Lin, W.-R. Wang, C.-C. Yang, S.-K. Chen, S.-J. Lin and J.-W. Yeh, *Intermetallics*, 2015, **62**, 76–83.
15 X. Guo, J. Wang, Z. Geng, Z. He, J. Peng, Z. Xu, W. Li and C. Wang, *J. Mater. Res. Technol.*, 2025, **35**, 4427–4437.
16 Z. Geng, J. Peng, W. Lu, Z. Xu, Q. Shen, C. Wang and L. Zhang, *J. Alloys Compd.*, 2025, **1036**, 181708.
17 L. Bai, Y. Xiao, J. Wang, M. Xu, S. Wang, C. Wang and J. Peng, *RSC Adv.*, 2024, **14**, 1056–1061.
18 L. Wang, X. Li, H. Niu, L. Yang, M. Xu and J. Yi, *Met. Mater. Int.*, 2022, **28**, 2413–2421.
19 F. Stein and A. Leineweber, *J. Mater. Sci.*, 2020, **56**, 5321–5427.
20 D. M. Cupid, M. J. Kriegel, O. Fabrichnaya, F. Ebrahimi and H. J. Seifert, *Intermetallics*, 2011, **19**, 1222–1235.
21 Y. Liang, C. Guo, C. Li and Z. Du, *J. Alloys Compd.*, 2008, **460**, 314–319.
22 J. Pavlů, J. Vřešťál and M. Šob, *Calphad*, 2010, **34**, 215–221.
23 M. Venkatraman and J. P. Neumann, *Bull. Alloy Phase Diagrams*, 1987, **8**, 216–220.
24 V. Jindal, B. N. Sarma and S. Lele, *Calphad*, 2013, **43**, 80–85.
25 X. J. Gao, L. Wang, N. N. Guo, L. S. Luo, G. M. Zhu, C. C. Shi, Y. Q. Su and J. J. Guo, *Int. J. Refract. Met. Hard Mater.*, 2021, **95**, 105405.
26 É. Fazakas, V. Zadorozhnyy, L. K. Varga, A. Inoue, D. V. Louzguine-Luzgin, F. Tian and L. Vitos, *Int. J. Refract. Met. Hard Mater.*, 2014, **47**, 131–138.
27 J. Wang, F. Jiang, L. Wang, G. Yang, M. Xu and J. Yi, *J. Alloys Compd.*, 2023, **946**, 169423.
28 L. Fang, J. Wang, X. Li, X. Tao, Y. Ouyang and Y. Du, *J. Alloys Compd.*, 2022, **924**, 166593.
29 Y. Zhang, H. Fu, J. He and J. Xie, *J. Alloys Compd.*, 2022, **891**, 162016.
30 O. N. Senkov, S. Gorsse and D. B. Miracle, *Acta Mater.*, 2019, **175**, 394–405.
31 N. N. Guo, L. Wang, L. S. Luo, X. Z. Li, Y. Q. Su, J. J. Guo and H. Z. Fu, *Mater. Des.*, 2015, **81**, 87–94.
32 W. Wang, Z. Zhang, J. Niu, H. Wu, S. Zhai and Y. Wang, *Mater. Today Commun.*, 2018, **16**, 242–249.
33 C. Xiang, E. H. Han, Z. M. Zhang, H. M. Fu, J. Q. Wang, H. F. Zhang and G. D. Hu, *Intermetallics*, 2019, **104**, 143–153.
34 Y. Zhang, T. T. Zuo, Z. Tang, M. C. Gao, K. A. Dahmen, P. K. Liaw and Z. P. Lu, *Prog. Mater. Sci.*, 2014, **61**, 1–93.
35 H. Huang, Y. Sun, P. Cao, Y. Wu, X. Liu, S. Jiang, H. Wang and Z. Lu, *Scr. Mater.*, 2022, **211**, 114506.
36 J. Yi, F. Cao, M. Xu, L. Yang, L. Wang and L. Zeng, *Int. J. Miner., Metall. Mater.*, 2022, **29**, 1231–1236.